applied sciences

MDPI

Article

Effects of Heat Treatment on the Microstructure and Hardness of A356 ($AlSi_7Mg_{0.3}$) Manufactured by Vertical Centrifugal Casting

Wonho Kim [1,2], Kyungsu Jang [3,*], Changwook Ji [2,*] and Eunkyung Lee [1,*]

[1] Department of Ocean Advanced Materials Convergence Engineering, Korea Maritime and Ocean University, Busan 49112, Korea; why355@naver.com
[2] Advanced Forming Process R&D Group, Korea Institute of Industrial Technology (KITECH), Ulsan 44776, Korea
[3] H/W Development, S-FAC Solution Factory, Daejeon 34025, Korea
* Correspondence: ksjang@s-fac.co.kr (K.J.); cwji@kitech.re.kr (C.J.); elee@kmou.ac.kr (E.L.); Tel.: +82-(051)-410-4353 (E.L.)

Abstract: The A356 alloy has been widely used in automotive components, such as wheels and brake disks, because it is an excellent lightweight material with high corrosion resistance and good mechanical properties. Recently, to reduce the weight of brake disks, the Fe-A356 hybrid brake disk has been suggested. Because brake disk quality is directly related to driving safety, the T4/T6 heat treatment of centrifugally cast A356 alloys were performed to enhance the mechanical properties and reduce micro-segregation. The solid-solution heat treatment followed by annealing caused the formation of Mg-rich intermetallic compounds on the grain boundaries of the Al matrix, decreasing the average hardness of the alloys by 13 HV. In contrast, the solid solution followed by water quenching (T4) reduced the area fractions of the intermetallic compounds and increased the average hardness by 11 HV. The T6 heat-treated A356 alloys, which were influenced by the formation of the Guinier–Preston zone exhibited a relatively higher average hardness, by 18 HV, compared to T4 heat-treated A356 alloys.

Keywords: A356 alloys; centrifugal casting; hardness; microstructure; heat treatment

check for updates

Citation: Kim, W.; Jang, K.; Ji, C.; Lee, E. Effects of Heat Treatment on the Microstructure and Hardness of A356 ($AlSi_7Mg_{0.3}$) Manufactured by Vertical Centrifugal Casting. *Appl. Sci.* **2021**, *11*, 11572. https://doi.org/10.3390/app112311572

Academic Editor: Filippo Berto

Received: 8 November 2021
Accepted: 1 December 2021
Published: 6 December 2021

1. Introduction

As exhaust emission standards and regulations have become increasingly strict, many automobile manufacturers have attempted to reduce vehicle exhaust emissions by improving power transmission efficiencies using several strategies, such as the reduction of the weight of vehicles and enhancement of the combustion process [1–3]. In particular, many automobile components, such as transmission cases, frame parts, and wheels, have been replaced with aluminum alloys because their light weight is beneficial to improve fuel efficiency and reduce exhaust emissions [4,5]. Among these components, the brake disk is one that has not been reduced in weight, and most of them are made of heavyweight cast iron [6,7].

Cast-iron brake disks are manufactured mainly by gravity casting; they are inexpensive and have an excellent wear resistance [8]. However, these disks have some problems with respect to the weights and poor heat dissipation performance, generating high temperatures during harsh driving conditions [9–11]. The high temperatures are likely to boil the brake oil and make a vapor within the brake piping system. This then triggers a vapor lock phenomenon that can cause a loss of braking capability [12,13]. In addition, the brake disk gets corroded by the dust generated from the brake pads and the exposure to the atmosphere. To tackle these problems, an Fe-A356 alloy brake disk was proposed using the vertical centrifugal casting method. Gray cast iron was used for the friction part that requires wear resistance. In other parts of the brake disk, A356 alloys, which are lighter than the gray cast iron and of higher thermal conductivity, were used to reduce the weight and improve the heat dissipation of the disk.

Unlike gravity casting, centrifugal casting is a method in which molten metal is injected during the rotation of the mold. It adheres to the mold wall by centrifugal force and then solidifies [14]. This casting process has been applied to the development of structural steel pipes, composite rolls, bearings, and cylinder liners. It has also been used broadly to produce functionally graded materials for special purposes [15–18]. The content of each solute atom depends on the particle densities and the rotational speed of the motor. For example, solute atoms that are heavier than the matrix alloy atoms move outward as the rotation speed increases. It is easy to segregate and to remove intermetallic compounds (IMCs) that act as impurities [18,19]. The materials fabricated via centrifugal casting possess a finer microstructure than those obtained via gravity casting, resulting in improved mechanical properties, such as the tensile strength, hardness, and fatigue limit [20].

The A356 alloy is widely applied in many automotive industries owing to its excellent castability and good mechanical properties [21,22]. The A356 alloy contains the eutectic Si, Mg_2Si, β-Al_5FeSi, and π-$Al_8Mg_3FeSi_6$. The Mg_2Si phases exhibit a transformation mechanism that changes from a supersaturated solution to a Mg and Si nanocluster formation, and then transforms into the Guinier–Preston (GP) zone, β″, β′ + Si, and finally to β. These phases could improve the mechanical properties of the material through artificial aging [23]. The β-Al_5FeSi phase generated at 841 K is needle-shaped, and its hardness and brittleness degrade its tensile strength and elongation [24]. The π-$Al_8Mg_3FeSi_6$ phase generated at 823 K has a Chinese script-like shape, which inhibits the formation of β-Al_5FeSi and improves the tensile strength [25,26]. During the heat treatment, the eutectic Si undergoes three morphological transformations, which change from fragmentation to spheroidization and finally to coarsening. Some researchers have reported that the more circular the eutectic Si, the greater the tensile strength and elongation [27].

In brake disks manufactured via the centrifugal casting process, the presence of the non-uniform IMC fraction in some parts, owing to the centrifugal force, adversely affects the safety and reliability of the brake disks. To solve this problem, heat treatment is required to improve the mechanical strength of the A356 alloy and to alleviate segregation during solidification. However, there are limited studies on the effects of heat treatment on centrifugally cast A356 aluminum alloys, and related experimental data are insufficient. Therefore, the effects of heat treatment, such as solid solution and artificial aging, on the microstructure and mechanical properties of A356 alloys produced by centrifugal casting were investigated in this study.

2. Theory

Particles in a viscous solution under a centrifugal force are subjected to radial centrifugal and viscous drag forces, which act in opposite directions. Therefore, Equation (1), which defines Stokes' law, explains the motion of the particles within the viscous solution [15], where $\frac{d^2x}{dt^2}$ is the acceleration, $\frac{dx}{dt}$ is the velocity, m is the mass, D_p is the particle diameter, ρ_p is the density of the particle, ρ_m is the density of the matrix, η is the viscosity coefficient, and G_g is the ratio between the rotational force and gravity (m/s^2).

$$m_p \frac{d^2x}{dt^2} = \left|\rho_p - \rho_m\right| \frac{4}{3}\pi \left(\frac{D_p}{2}\right)^3 G_g - 3\pi\eta D_p \frac{dx}{dt} \tag{1}$$

The value of G_g can also be defined as in Equation (2), where r is the diameter of the cast ring (m), N is the rotational velocity (rpm), and g is the gravitational acceleration.

$$G_g = \frac{r}{g}\left(\frac{2\pi N}{60}\right)^2 \tag{2}$$

During centrifugal casting, several different events occur simultaneously because of the flow of the molten metal and the surrounding environment in the mold. To express Equation (2) in terms of the centripetal acceleration (a_p) and particle densities only, the equation is expressed in a simplified form as shown in Equation (3), ignoring the initial velocity and the radius of the particle. A negative value of a_p signifies that the particles move towards the center of rotation.

$$a_p = \frac{\rho_p - \rho_m}{\rho_p} 4\pi^2 N^2 r \tag{3}$$

To determine the influence of density on the behavior of the solute atoms (Table 1), their densities were used in Equation (3). Si and Mg, which are less dense than Al, move toward the center of rotation, while Fe, which is approximately 2.9 times denser than Al, moves away. The a_p of Fe, Si, and Mg were 25.813, −6.866, and −21.781 rN^2, respectively. Thus, the a_p of Fe is 3.76 and 1.18 times larger in magnitude than those of Si and Mg, respectively.

Table 1. Density of solute atoms in the A356 alloy.

	Al	Si	Mg	Fe
Density (g/cm^3)	2.7	2.3	1.74	7.8

3. Materials and Methods

3.1. Sample Preparation

A schematic of the vertical centrifugal casting process performed in this experiment is shown in Figure 1. After inserting the round gray cast iron into a mold, the mold was preheated to 673 K and then rotated at 230 rpm. A molten aluminum alloy at 953–963 K was then poured into the mold and the rotation was stopped after 80 s. Finally, a gray cast-iron A356 alloy brake disk was manufactured through the process of age hardening for 200 s in the mold. An optical emission spectrometer was used to measure the aluminum alloy content used in the brake disk body as Al: bal, Si: 6.8 wt.%, Mg: 0.37 wt.%, Fe: 0.14 wt.%, Ti: 0.09 wt.%, Cu: 0.04 wt.% and Sr: 95 ppm. The schematic of the hybrid brake disk and the locations A and B for hardness and microstructure investigations in this casting is shown in Figure 2. Section A is closer to the center than section B; both sections correspond to the outermost locations under the pressure of the brake pads.

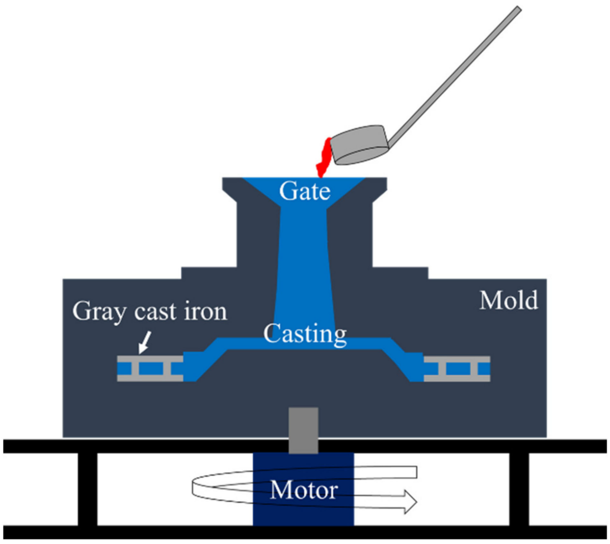

Figure 1. Schematic of vertical centrifugal casting apparatus used in this experiment. Rotation direction is counterclockwise.

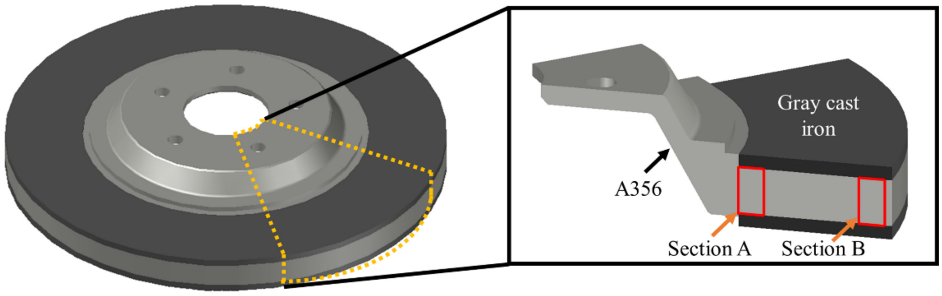

Figure 2. Schematic of gray cast iron–A356 hybrid brake disk after casting; investigated locations in brake disk are highlighted. Section A is closer to the center of rotation than section B.

3.2. Heat Treatment

To investigate the effects of heat treatment on the mechanical properties of this material, a solid solution treatment (ST) was performed at 773 K for 4 h with several different cooling media, such as annealing (E) and water quenching (WQ). Artificial aging (AG) was performed at 473 K for 4 h with WQ. In the current study, solid-solution and artificial-aging heat treatments are referred to as ST and AG hereafter, respectively. Moreover, ST-E represents annealing after ST, and ST-WQ represents water quenching after ST. ST-WQ-AG represents to be performed the artificial aging after ST-WQ. The ST-WQ and ST-WQ-AG processes are the T4 and T6 heat treatments, respectively. The cooling rate related to this heat treatment was measured using an in-situ software, as shown in Table 2.

Table 2. Heat treatment condition of A356 alloys (based on at 298 K).

Heat Treatment		Temperature (K)	Holding Time (h)	Heating Rate (K/min)	Cooling Rate (K/min)
ST	E	773	4	4.16	1.1
	WQ				1340
AG		473	4	1.67	1750

3.3. Microhardness Test

The A356 alloys were subjected to micro-hardness testing (HM-122, Akashi, Japan) under a pressure of 0.05 kgf/cm^2 held for 10 s. All samples from sections A and B were measured 20 times, and the values were averaged, excluding the maximum and minimum values.

3.4. Differential Scanning Calorimetry (DSC)

The samples were treated with the solid solution for 10 h at 813 K, followed by cooling at different rates (water quenching and annealing) to analyze the strengthening mechanism after the AG heat treatment. Subsequently, 13 $\pm$ 0.5 mg of each sample was cut and placed in a pellet-shaped capsule. Differential scanning calorimetry (DSC; N-650, SCINCO.) was performed at a heating rate of 50 K/min in a 40 cc/min flow of Ar.

3.5. Microstructural Analysis

All samples were polished with 200 to 2400-grit silicon carbide papers and with a 0.25 µm diamond suspension and a 0.04 µm colloidal suspension. These samples were observed with an optical microscope (OM; Eclipse LV150N, Nikon Metrology Inc., Tokyo, Japan) and a field emission scanning electron microscope (FE-SEM; MIRA3, Tescan.—Brno, Czech Republic) with an acceleration voltage of 5.0 kV. Energy dispersive spectroscopy (EDS, EDAX, Mahwah, NJ, USA) was also performed to analyze the chemical composition of IMCs. Chemical quantitative analysis was performed using an electron probe microanalyzer (EPMA; JXA-8230, JEOL Ltd.—Tokyo, Japan) with an acceleration voltage of 15.0 kV. The area fractions of the IMCs and microstructures were measured using an image analyzer (I-solution DT software).

4. Results and Discussion

4.1. Microstructure of Sections A and B before Heat Treatment

Figure 3 shows the non-heated A365 alloy samples from sections A and B. The microstructural characteristics of each section, such as the IMC distributions, were significantly different. The crosslines in the images are examples of measurements of the secondary dendrite arm spacing (SDAS) based on ASTM E112–96 (Reapproved 2004). The average SDAS values in sections A and B were 51.85 and 35.04 μm, respectively. The microstructure of section A was coarser than that of section B. The solidification rate of each section was calculated using Equation (4), where V is the solidification rate [28]. The solidification rate in Section B was determined as 87 K/s, which was 3.45 times higher than that in Section A (25 K/s).

$$\mathrm{SDAS} = 39.4\mathrm{V}^{-0.317} \tag{4}$$

When the microstructure is affected by rotational force, IMCs are observed opposite the center of rotation. In contrast, more IMCs were observed in section A than in section B. This indicates that the microstructure was less affected by rotation force than by the solidification rate. Thus, the Fe-rich IMCs were more concentrated in section A owing to its lower solidification rate. The Fe-rich IMCs were distributed adjacent to the dendrite owing to their low solubilities in the Al matrix. These compounds experienced difficulty in escaping from the dendrite, thereby causing micro-segregation. The IMCs were impurities on the A356 alloys, therewith degrading the mechanical properties [24].

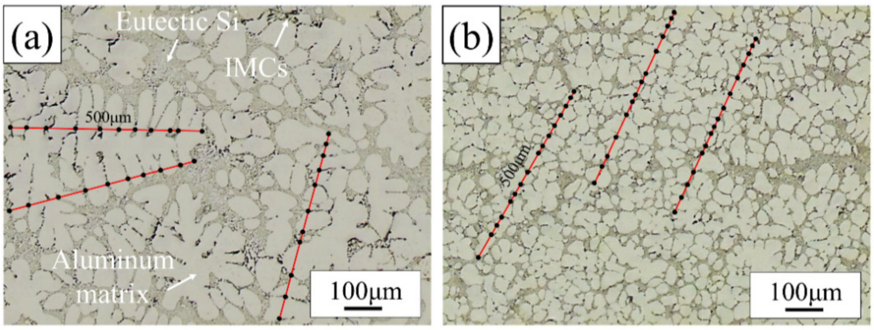

Figure 3. Optical microscopy images of non-heated A356 alloy; crosslines in the images indicate measurements of secondary dendrite arm spacing. (**a**) section A and (**b**) section B. Section A is closer to the center of rotation than section B.

4.2. Effects of Heat Treatment on the A356 Alloys

Figure 4 shows the microstructures of the A365 alloys after heat treatment. Compared to the non-heated A356 alloys (Figure 3), the Fe-rich IMCs adjacent to the dendrite decreased in ST-WQ. When ST-E was used, the contents of the Fe-rich IMCs were similar to those in the non-heated A356 alloys. Figure 5a shows the SDAS measured using the linear intercept method (crossline in Figure 3). Depending on the heat treatment, the SDAS in sections A and B did not change significantly. However, they varied according to the cooling rates after ST and grew slightly, even with AG. Figure 5b shows the area fractions of the intermetallic compounds. The area fractions of the IMCs decreased in the samples with WQ after ST. In contrast, the area fractions of the IMCs in the ST-E A356 alloys was similar to that in the non-heated A356 alloys. In the ST-WQ and ST-WQ-AG A356 alloys, the difference of area fraction between sections A and B was decreased from 0.42% to 0.2% (compared to that in the non-heated A356 alloys). The reductions of the area fraction and the difference of area fraction occurred because the Mg constituting the π-$Al_8Mg_3FeSi_6$ phases was re-dissolved into the Al matrix during ST [29]. The aspect ratio about the horizontal axis/vertical axis of eutectic Si was shown in Figure 5c; if the value were closer to 1, it would adopt a more spherical shape. As a result of the ST, the aspect ratio of eutectic Si decreased by approximately 0.3 compared to that of the non-heated A356 alloys. This was because inter-diffusion occurred to reduce the surface energy of the Si solute atoms owing to the driving force during the heat treatment [27]. The spheroidization of eutectic Si in heat-treated A356 alloys yielded a similar aspect ratio.

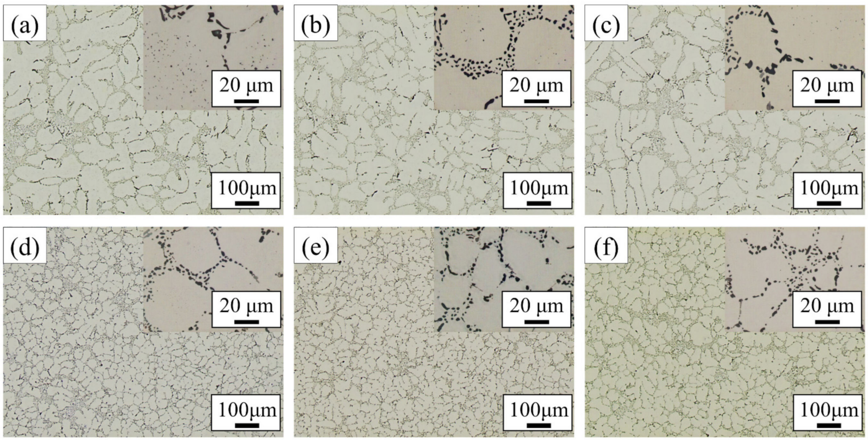

Figure 4. Optical microscopy images of heat-treated A356 alloy: (**a**–**c**) section A; (**d**–**f**) section B; (**a**,**d**) ST-E, (**b**,**e**) ST-WQ, and (**c**,**f**) ST-WQ-AG (section A is closer to the center of rotation than section B).

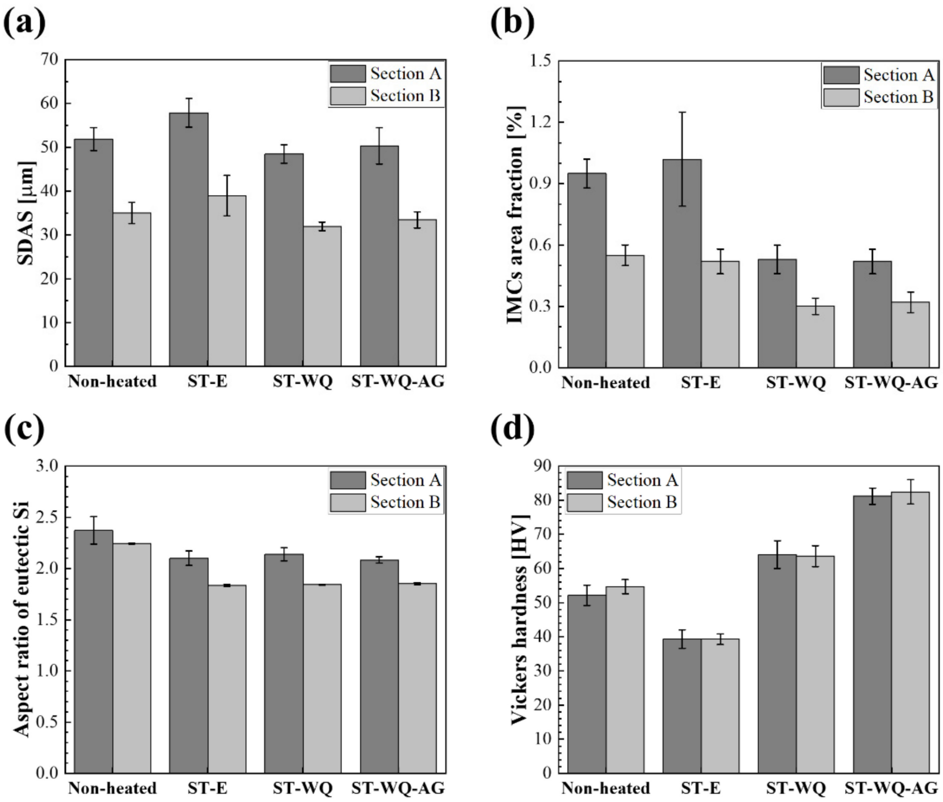

Figure 5. Quantitative microstructural analysis using I-solution DT image software: (**a**) SDAS, (**b**) area fraction of IMCs, (**c**) aspect ratio of eutectic Si, and (**d**) Vickers hardness.

Figure 5d shows the Vickers hardness values of both sections after heat treatment. In both sections the HV values were similar because the values existed within deviation ranges. The differences are observed between the specific heat treatment processes. The average hardness was calculated to this Equation ((section A + section B)/2). Compared to the non-heated A356 alloys, the average hardness of the ST-E A356 alloys decreased by 13 HV because of grain boundary segregation caused by the formation of eutectic-Mg_2Si adjacent to eutectic Si and π-AlMgFeSi [30]. In contrast, the average hardness of the ST-WQ A356 alloys were 64 HV, which were higher than the non-heated A356 alloys. These changes corresponded to the reduction in the area fractions of IMCs that occurred as Mg solute atoms re-dissolved into the Al matrix during ST. This led to the solid-solution strengthening effect owing to the re-dissolution of Mg in the Al matrix.

4.3. Analysis of IMCs

Figure 6 shows the quantitative analysis of section B. The A356 alloy contained eutectic Si phases and Fe-rich IMCs (π-AlMgFeSi, β-FeSiAl) around the Al matrix. The Fe-rich IMCs were identified by EDS and were divided into a gray π-AlMgFeSi and a needle-shaped light-gray β-FeSiAl phase (Figure 7c). After ST-WQ and ST-WQ-AG, π-AlMgFeSi phases were transformed into β-FeSiAl phases owing to the low melting temperature of the Mg solute atoms. Differences in the sizes and morphologies of the β-FeSiAl phases were not observed. The eutectic Si in the non-heated A356 alloys was present with a relatively uniform concentration. However, the concentrations of Si solute atoms constituting the π-AlMgFeSi and β-FeSiAl phases were slightly increased.

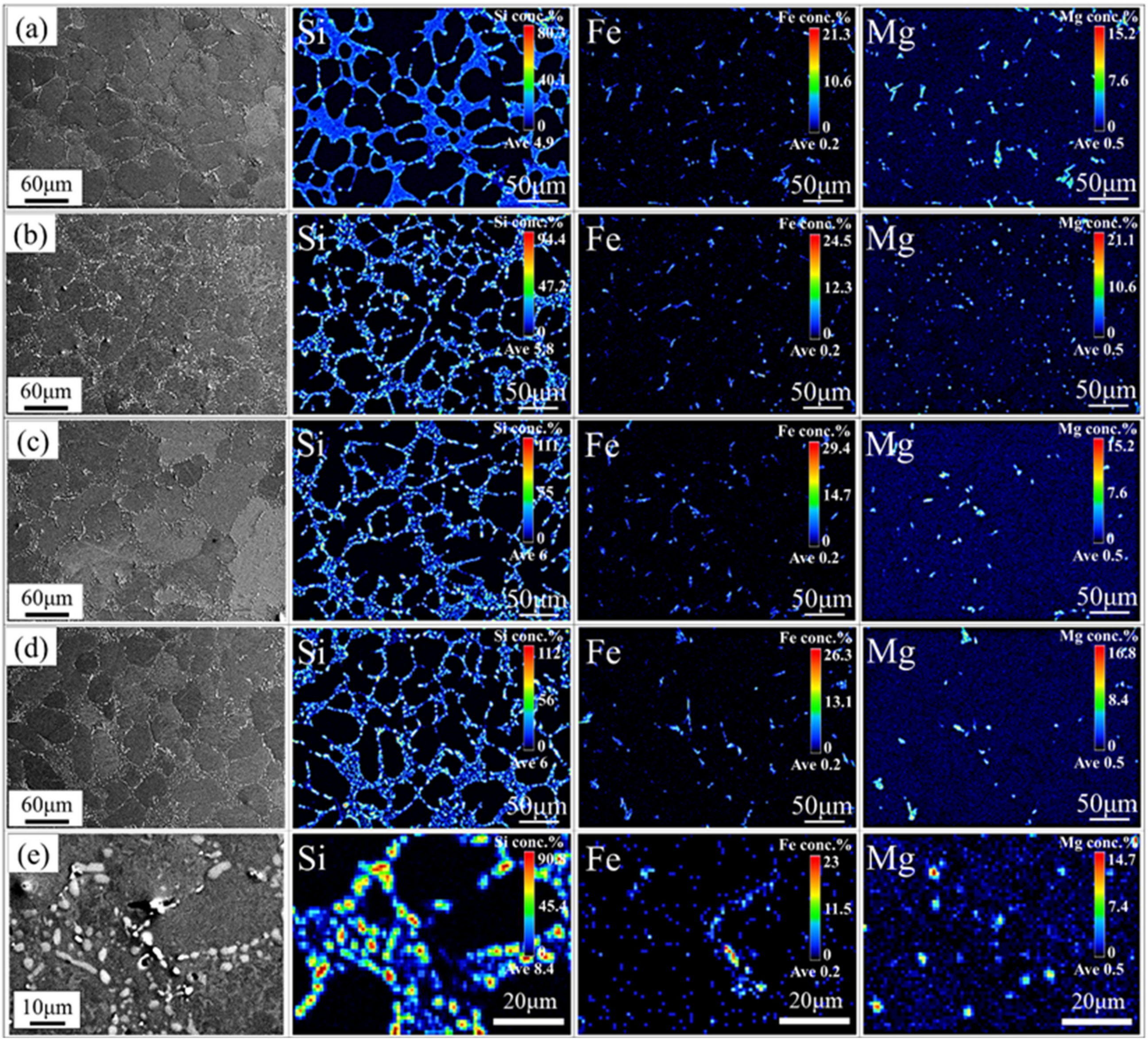

Figure 6. Secondary electron images and chemical element quantitative mapping obtained by EPMA in section B: (**a**) non-heated, (**b**) ST-E, (**c**) ST-WQ, and (**d**) ST-WQ-AG samples, (**e**) magnifications of (**b**).

Table 3. Qualitative analysis (EDS/EDAX) results of points in Figure 7 (wt.%).

Point	Al	Si	Mg	Fe
1	77.04	16.75	-	6.22
2	84.71	14.26	1.02	-
3	75.55	20.16	4.29	-
4	49.06	26.78	14.34	9.83
5	71.94	11.20	-	16.87

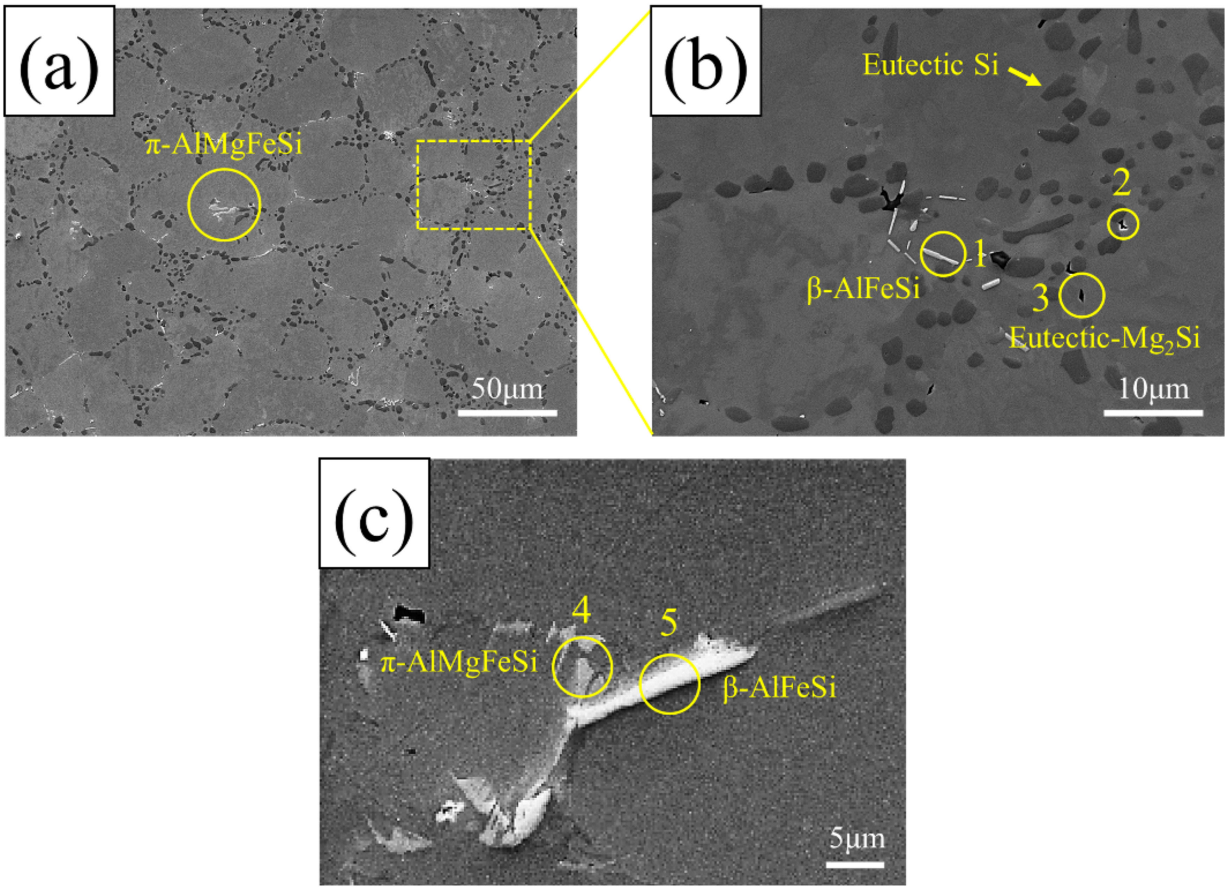

Figure 7. Field-emission scanning microscopy images of samples after ST-E heat treatment: (**a**,**b**) located in section B, and (**c**) representative phases of π-AlMgFeSi and β-FeSiAl in these A356 alloys. Chemical compositions of these points are shown in Table 3.

After the ST-WQ, the microstructure was relatively finer than before heat treatment, and the solute micro-segregation of Si solute atoms was reduced. The Mg solute micro-segregation distributed in the Si and Fe are shown in Figure 6b. These corresponded to the concentrated Mg solute atoms, as shown in Figure 7 (Points 2 and 3). The microstructures of the ST-WQ and ST-WQ-AG A356 alloys were not significantly different, as shown in Figure 6c,d. However, the hardness in section A increased from 64.1 HV to 81.2 HV, and in section B from 63.7 HV to 82.5 HV (Compared to the ST-WQ and ST-WQ-AG A356 alloys).

Figure 8 shows the DSC analytical results of the precipitation and dissolution of the phases. In general, DSC is used to observe the temperatures at which fine phases are precipitated. The convex upward peak is an exothermic peak when a phase is formed, and the concave downward peak is an endothermic peak when the phase is re-dissolved into the Al matrix. An exothermic peak around 400 K is known as the Guinier–Preston zone (GP zone). In this zone, a fine-scale metallurgical phenomenon of Mg–Si nanocluster formation occurs [31]. The exothermic peaks between 500 and 600 K were generated by the formation of β″ and β′ phases [32]. The values of the entropy/heat of reaction are calculated by this method [33]. A higher entropy value means that a lot of phases have been formed. When considering the temperature of artificial aging, the increase of average hardness in ST-WQ-AG A356 alloys by 18 HV compared to the ST-WQ A356 alloys was determined to be because of a precipitation-strengthening effect that occurred by the formation of the GP zone in the Al matrix.

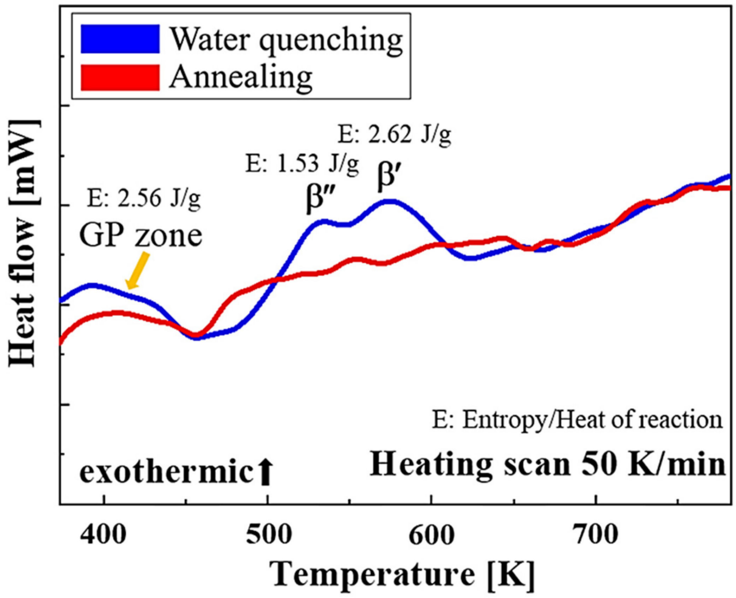

Figure 8. DSC curve of A356 alloy (water quenching and annealing after ST at 813 K for 10 h).

5. Conclusions

This research was aimed at increasing the quality of centrifugally cast A356 alloys by improving the mechanical properties and reducing segregation caused by the Fe-rich IMCs through heat treatment.

1. Concerning the non-heated A356 alloys, the SDAS of section A was 1.48 times coarser than section B, and the area fraction of Fe-rich IMCs in section A (0.95%) was 1.72 times higher than that in section B. This difference in microstructure of sections A and B can be reduced through heat treatment.
2. The SDAS in the ST-E heat-treated A356 alloys was longer than that in the non-heated A356 alloys by 3.92 μm, and the eutectic-Mg_2Si phases were precipitated at the grain boundaries. This phase caused grain boundary segregation and decreased the average hardness by 13 HV. The differences in the area fractions of Fe-rich IMCs between section A and section B were similar to those from before heat treatment.
3. In the ST-WQ (T4) heat-treated A356 alloys, the SDAS was decreased by 3.1 μm, compared to the non-heated alloys. In addition, the area fraction of the Fe-rich IMCs decreased by 0.25. This decrease occurred because the Mg solute atoms included in the π-AlMgFeSi phases were re-dissolved into an aluminum matrix. This caused the average hardness to increase by 11 HV. Moreover, the difference in area fraction of Fe-rich IMCs between section A and section B was reduced from 0.42% to 0.2%.
4. The segregation of Si and Mg solute atoms was reduced by ST-WQ and ST-WQ AG. The average hardness of the ST-WQ-AG (T6) heat-treated A356 alloys was the highest value owing to GP zone formation during artificial aging.

This study presented the potential for the heat treatment of aluminum alloys manufactured by vertical centrifugal casting processes. The consequence would guarantee the quality of castings by reducing segregation and improving mechanical properties, and would be a reference for optimizing heat treatment of aluminum alloys manufactured by the vertical centrifugal casting.

Author Contributions: Conceptualization, W.K. and E.L.; methodology, W.K and C.J.; visualization, W.K.; validation, C.J., K.J. and E.L.; formal analysis, W.K. and E.L.; investigation, W.K. and E.L.; resources, K.J.; data curation, W.K.; writing—original draft preparation, W.K.; writing—review and editing, K.J., E.L. and C.J.; project administration, E.L. and C.J.; funding acquisition, E.L. and C.J. All authors have read and agreed to the published version of the manuscript.

Funding: This research was supported by the National Research Foundation of Korea (NRF) granted by the Korean Government (NRF-2019R1I1A3A01062863). And this study has been financially supported by the Ministry of Economy and Finance and conducted with the support of the Korea Institute of Industrial Technology as "Development of Smart Manufacturing Technology for Low Temperature Fuel Tank for LNG Ships project KITECH JA210008".

Institutional Review Board Statement: Not applicable.

Informed Consent Statement: Not applicable.

Data Availability Statement: The data presented in this study are available on request from the corresponding author.

Conflicts of Interest: The authors declare no conflict of interest.

References

1. Cuenot, F. CO2 emissions from new cars and vehicle weight in Europe; How the EU regulation could have been avoided and how to reach it? *Energy Policy* **2009**, *37*, 3832–3842. [CrossRef]
2. Parekh, H.; Ramani, B.; Parekh, C. Performance Enhancement of Internal Combustion Engine Using Weight Reduction Approach. *Int. J. Automot. Mech. Eng.* **2018**, *15*, 4962–4977. [CrossRef]
3. Villanueva-Rey, P.; Belo, S.; Quinteiro, P.; Arroja, L.; Dias, A.C. Wiring in the automobile industry: Life cycle assessment of an innovative cable solution. *J. Clean. Prod.* **2018**, *204*, 237–246. [CrossRef]
4. Hirsch, J. Recent development in aluminium for automotive applications. *Trans. Nonferrous Met. Soc. China* **2014**, *24*, 1995–2002. [CrossRef]
5. Ahn, C.; Lee, E. Effect of cooling rate on the corrosion resistance and mechanical property of AlSi10MnMg alloy. *J. Adv. Mar. Eng. Tech.* **2019**, *43*, 618–624. [CrossRef]
6. Maleque, M.A.; Dyuti, S.; Rahman, M.M. Material selection method in design of automotive brake disc. *WCE 2010 World Congr.* **2010**, *3*, 2322–2326.
7. Le Gigan, G.; Ekh, M.; Vernersson, T.; Lundén, R. Modelling of grey cast iron for application to brake discs for heavy vehicles. *Proc. Inst. Mech. Eng. Part D J. Automob. Eng.* **2017**, *231*, 35–49. [CrossRef]
8. Cueva, G.; Sinatora, A.; Guesser, W.L.; Tschiptschin, A.P. Wear resistance of cast irons used in brake disc rotors. *Wear* **2003**, *255*, 1256–1260. [CrossRef]
9. Talati, F.; Jalalifar, S. Analysis of heat conduction in a disk brake system. *Heat Mass Transf. Stoffuebertragung* **2009**, *45*, 1047–1059. [CrossRef]
10. Shaik, A.F.B.; Srinivas, C.L. Structural and thermal analysis of disc brake with and without crossdrilled rotar of race car. *Int. J. Adv. Eng. Res. Stud.* **2012**, *4*, 39–43.
11. Ormerod, J.; Taylor, R.; Edwards, J.R. Thermal diffusivity of cast irons. *Met. Technol.* **1978**, *5*, 109–113. [CrossRef]
12. Atwood, D.H.; Ferrara, G. Vapor lock studies for gasolines with ethers. *SAE Tech. Pap.* **1993**. [CrossRef]
13. Radlinski, R.W.; Forthofer, R.J.; Harvey, J.L. Operating performance of motor vehicle braking systems as affected by fluid water content. *SAE Tech. Pap.* **1971**, 1037–1045. [CrossRef]
14. Song, N.; Luan, Y.; Bai, Y.; Xu, Z.A.; Kang, X.; Li, D. Numerical Simulation of Solidification of Work Roll in Centrifugal Casting Process. *J. Mater. Sci. Technol.* **2012**, *28*, 147–154. [CrossRef]
15. Rahvard, M.M.; Tamizifar, M.; Boutorabi, S.M.A.; Gholami Shiri, S. Characterization of the graded distribution of primary particles and wear behavior in the A390 alloy ring with various Mg contents fabricated by centrifugal casting. *Mater. Des.* **2014**, *56*, 105–114. [CrossRef]
16. Koizumi, M.; Niino, M. Overview of FGM Research in Japan. *MRS Bull.* **1995**, *20*, 19–21. [CrossRef]
17. Gao, J.W.; Wang, C.Y. Modeling the solidification of functionally graded materials by centrifugal casting. *Mater. Sci. Eng. A* **2000**, *292*, 207–215. [CrossRef]
18. Madhusudhan; Narendranath, S.; Kumar, G.C.M.; Mukunda, P.G. Experimental study on rate of solidification of centrifugal casting. *Int. J. Mech. Mater. Eng.* **2010**, *5*, 101–105.
19. Zhang, W.Q.; Yang, Y.S.; Zhu, Y.F.; Liu, Q.M.; Hu, Z.Q. Structural transition and macrosegregation of Al-Cu eutectic alloy solidified in the electromagnetic centrifugal casting process. *Metall. Mater. Trans. A Phys. Metall. Mater. Sci.* **1998**, *29*, 404–408. [CrossRef]
20. Chirita, G.; Soares, D.; Silva, F.S. Advantages of the centrifugal casting technique for the production of structural components with Al-Si alloys. *Mater. Des.* **2008**, *29*, 20–27. [CrossRef]

21. Sanders, R.E. Technology innovation in aluminum products. *JOM* **2001**, *53*, 21–25. [CrossRef]
22. Becker, M.N. Aluminum: New Challenges in Downstream Activities. *JOM* **1999**, *51*, 26–38. [CrossRef]
23. Belov, N.A. Industrial Casting Aluminum Alloys. In *Casting Aluminum Alloys*; Elsevier: Amsterdam, The Netherlands, 2007; Chapter 5; pp. 327–396. ISBN 9780080453705.
24. Gencalp Irizalp, S.; Saklakoglu, N. Effect of Fe-rich intermetallics on the microstructure and mechanical properties of thixoformed A380 aluminum alloy. *Eng. Sci. Technol. Int. J.* **2014**, *17*, 58–62. [CrossRef]
25. Fortini, A.; Merlin, M.; Fabbri, E.; Pirletti, S.; Garagnani, G.L. On the influence of Mn and Mg additions on tensile properties, microstructure and quality index of the A356 aluminum foundry alloy. *Procedia Struct. Integr.* **2016**, *2*, 2238–2245. [CrossRef]
26. Wang, Q.G. Microstructural effects on the tensile and fracture behavior of aluminum casting alloys A356/357. *Metall. Mater. Trans. A Phys. Metall. Mater. Sci.* **2003**, *34*, 2887–2899. [CrossRef]
27. Lin, Y.C.; Luo, S.C.; Huang, J.; Yin, L.X.; Jiang, X.Y. Effects of solution treatment on microstructures and micro-hardness of a Sr-modified Al-Si-Mg alloy. *Mater. Sci. Eng. A* **2018**, *725*, 530–540. [CrossRef]
28. Wang, Q.G.; Apelian, D.; Lados, D.A. Fatigue behavior of A356/357 aluminum cast alloys. Part II—Effect of microstructural constituents. *J. Light Met.* **2001**, *1*, 85–97. [CrossRef]
29. Boettinger, W.J.; Kattner, U.R. Analysis of Solidification Path and Microsegregation in k (V). *Model. Cast. Weld. Adv. Solidif. Process.* **1998**, *8*, 159–170.
30. Taylor, J.A.; St John, D.H.; Barresi, J.; Couper, M.J. Influence of Mg content on the microstructure and solid solution chemistry of Al-7%Si-Mg casting alloys during solution treatment. *Mater. Sci. Forum* **2000**, *331*, 277–282. [CrossRef]
31. Manickaraj, J.; Liu, G.; Shankar, S. Effect of incubation coupled with artificial aging in T6 heat treatment of A356.2 aluminum casting alloy. *Int. J. Met.* **2011**, *5*, 17–34. [CrossRef]
32. Lee, E.; Walde, C.; Mishra, B. Effects of Cooling Rate on Precipitate Evolution and Residual Stresses in Al–Si–Mn–Mg Casting Alloy. *Met. Mater. Int.* **2018**, *24*, 815–820. [CrossRef]
33. Tan, Y.H.; Lee, S.L.; Lin, Y.L. Effects of Be and Fe additions on the microstructure and mechanical properties of A357.0 alloys. *Metall. Mater. Trans. A* **1995**, *26*, 1195–1205. [CrossRef]